coatings

MDPI

Article

All-Solid-Waste-Derived High-Temperature Ceramic Glazes Enable Mechanism-Informed Sustainable Color and Texture Design via Phase–Microstructure Tuning

Yixuan Du [2], Lanlan Cheng [2], Yumeng Huang [3], Minxuan Chen [2] and Haoran Li [1,*]

[1] School of Arts, Sun Yat-sen University, Guangzhou 510275, China
[2] Beijing Institute of Technology, School of Design & Arts, Beijing 100081, China; 6120240012@bit.edu.cn (Y.D.)
[3] Hebei Fine Arts Publishing House, Shijiazhuang 050700, China
* Correspondence: ihr83@mail.sysu.edu.cn

Abstract

Glazes primarily utilize raw minerals like kaolinite. However, considering sustainable development, employing industrial solid waste offers greener design solutions and high economic efficiency. This study employs multiple analytical methods, including XRF, XRD, and SEM, to investigate the feasibility of replacing traditional glaze materials entirely with solid waste. It elucidates the mechanisms underlying changes in texture and color resulting from alterations in microstructure and chemical composition. Research on five different ratios of ceramic glaze composed of fly ash, blast furnace slag, silica fume, coal gangue, and desulfurization gypsum reveals that the implementation of solid waste-based glazes is feasible. The glazes formed a SiO_2–Al_2O_3–CaO system surface, all exhibiting anorthite and diopside as the primary crystalline forms. The results are as follows: 1. The content of Ca and Mg depends on the overall proportion of elements, with a Ca threshold of approximately 28%. Below this threshold, characteristics such as surface roughness and porosity are observed. Above this threshold, as seen in G3 and G4, crystal distribution becomes more dense. 2. Si is the key factor controlling crystal variation. Sample G5 exhibits good crystal continuity. Visually, its color appears distinctly deep red. 3. Samples G1 and G2 both contain approximately 4.8 wt% Fe_2O_3, but G2 exhibits more crystalline precipitation. Visually, G2 appears more reddish-yellow than G1. Higher crystallinity yields superior coloration.

Keywords: industrial solid waste; waste-derived ceramic glazes; all-solid-waste-derived; microstructure; sustainable materials; appearance engineering

Academic Editor: Csaba Balázsi

Received: 16 March 2026
Revised: 6 April 2026
Accepted: 9 April 2026
Published: 13 April 2026

1. Introduction

With industrial development, while providing convenience for human life, it has also generated various types of industrial solid waste [1]. Among these wastes, industrial residues such as fly ash, blast furnace slag, coal gangue, and desulfurization gypsum continue to exert significant pressure on the environment [2,3]. The rational disposal of these wastes has become a core concern [4].

Colorants and transparent glazes primarily determine the texture and color of ceramic glazes. The production of glazes typically employs natural raw materials, and the extensive use of these materials necessitates the extraction of high-quality mineral resources. The ecological damage and energy consumption associated with mining operations further contribute to carbon emissions.

Among the primary chemical constituents present in ceramic raw materials, SiO_2 functions as the principal modifier in glaze compositions, controlling characteristics such as translucency, matte finish, and opacity [5]. TiO_2 acts as the flow medium within the glaze [6]. Al_2O_3 forms the microstructure of ceramic glazes [7]. Additionally, inorganic pigments, such as Fe_2O_3 and SnO_2, interact to produce the ultimate aesthetic effect of ceramic glazes [8].

Solid waste contains various chemical components such as SiO_2, Al_2O_3, CaO, and Fe_2O_3, all of which are primary materials for forming ceramic glazes [9]. Research on reusing solid waste as additives in ceramics has been ongoing for some time, encompassing applications such as transparent ceramic glazes, ceramic tableware, ceramic tiles, and porous structured ceramics [10–12]. Furthermore, this approach is increasingly being applied to the design of household ceramics and the study of affect mechanisms [13,14].

However, solid waste primarily functions as an additive or partial substitute for conventional materials. This relatively low utilization rate and complex application methods remain regrettable. Examples include retorted shale as a pigment additive in ceramic glazes and the use of furnace slag (ZnO) in coloring formulations for wall tile glazes [15,16]. Additionally, leather solid waste has been employed as a chromium precursor system, and in terms of substituting and incorporating ceramic body raw materials, rice husk ash (RHA) has been used to replace SiO_2 [17,18].

This method has been used to make ceramic glazes with fly ash instead of kaolin, high-strength ceramics with blast furnace slag, glass-ceramics with coal gangue, and foam glass-ceramics with desulfurization gypsum [19–23]. Studies have shown that these additives work well in ceramic applications. In addition, more studies like utilizing urban waste such as roof tiles as clay base materials and marble as glaze and body material for daily-use ceramics [10,24].

Recent studies increasingly indicate the potential for producing ceramic glazes from various combinations of solid waste materials [25–27]. However, while solid waste has been extensively tested as an additive in diverse ceramic forms, its application as a glaze component remains challenging. Directly incorporating 100% solid waste into ceramics is also rare, and specialized research quantifying effects such as color and texture is lacking. Current studies reveal limited research on the relationship between microstructure and macrostructure, as shown in Table 1.

Table 1. Current status of solid waste incineration for ceramic production.

Author/Journal	Solid Waste Firing	Temperature	Solid Waste Ratio	Effect
da Silva, R. C. et al. Ceramics International (2012) [28]	Limestone waste	800–1150 °C	25 wt%	Enhances hardness, renders glaze opaque
Hui, T. et al. Ceramics International (2022) [29]	Titanium slag, gold tailings waste	1180 °C	gold tailings 70 wt%	Promotes glaze pore growth
Sonia, M. et al. Science of Sintering (2025) [30]	Soda ash, lime, glass waste	1230 °C	7–20 wt%	Enhances flexural strength, hardness, whiteness, brightness
Koroglu, L. et al. Journal of the Australian Ceramic Society (2023) [9]	Boron Derivative Waste	950–1150 °C	5–15 wt%	High gloss, high whiteness
Du, Y. X. et al. Sustainability (2025) [19]	Fly ash	1270 °C	27–29 wt%	Replaces kaolin to regulate glaze texture

Specific difficulties include the varying compositions of different solid wastes, which complicate the addition process. The variation in proportions of multiple waste materials exhibits high complexity [31,32]. Crystalline transformations and stability within glass systems pose challenges for chemical composition analysis [25]. This phenomenon leads to glaze defects such as uneven glazing and cracking [33]. Trace elements and residual elements are critical for controlling crystalline characterization [34]. However, crystals can also be influenced by other processes like heat treatment [35]. Consequently, these factors ultimately impact the commercial conversion of solid waste into ceramic applications [36]. These studies not only highlight the challenges encountered when utilizing solid waste in ceramic applications but also serve as experimental hypotheses regarding solid waste as a complete additive for ceramic glazes. The actual effectiveness in practical application remains unclear.

From an additive perspective, numerous studies have also utilized fly ash as a substrate [33,37]. However, excessive fly ash content prevents the formation of glass-ceramics without supplementary silica materials [38]. Similarly, extensive use of coal gangue hinders ceramic formation and yields results with insignificant variance, complicating observational analysis [39,40].

We conducted a systematic analysis of the chemical composition and traditional techniques of ceramic glaze materials. This study investigates the effects of incorporating different solid waste materials on the oxide composition, phase structure, and microstructure. It explores the impact of varying solid waste ratios on these properties and identifies suitable formulations. Specifically: first, we systematically analyzed the silicate ratios in the ceramic glaze base, along with the combustion aids and colorants. Utilizing 100% solid waste materials, the parameter range is designed based on the "phase structure-microstructure-color/texture" framework. Then, we designed an experimental approach using fly ash, blast furnace slag, silica fume, coal gangue, and desulfurization gypsum as experimental materials. Five samples were designed with different ratios. Next, under identical firing conditions—including identical heating profiles, kiln batches, and porcelain clay—we completed firing at 1250 °C. The innovation lies in attempting to explore Ca-Mg threshold-driven crystallization and microstructural texturing pathways. Finally, we employed traditional analytical techniques, including XRD, XRF, and SEM, to characterize the chemical composition and physical properties of the samples.

This study investigates the fundamental composition of various solid wastes and attempts to address the following questions: 1. How do solid waste additives alter the key oxide ratios in glazes? 2. Which crystalline phases and degrees of crystallinity correspond to these compositional changes? 3. How does microstructure lead to differences in texture and appearance?

Figure 1 presents the conceptual roadmap of our research. First, the incorporation of fly ash induces changes in the composition of calcium, aluminum, silicon, and other elements. Concurrently, this leads to variations in the proportions of different crystalline phases. Second, the microstructure is examined to observe grain and pore structures. Third, L*a*b* values and gloss are measured through light scattering and absorption. Ultimately, this establishes the structure–property relationship between "composition—structure—optical properties".

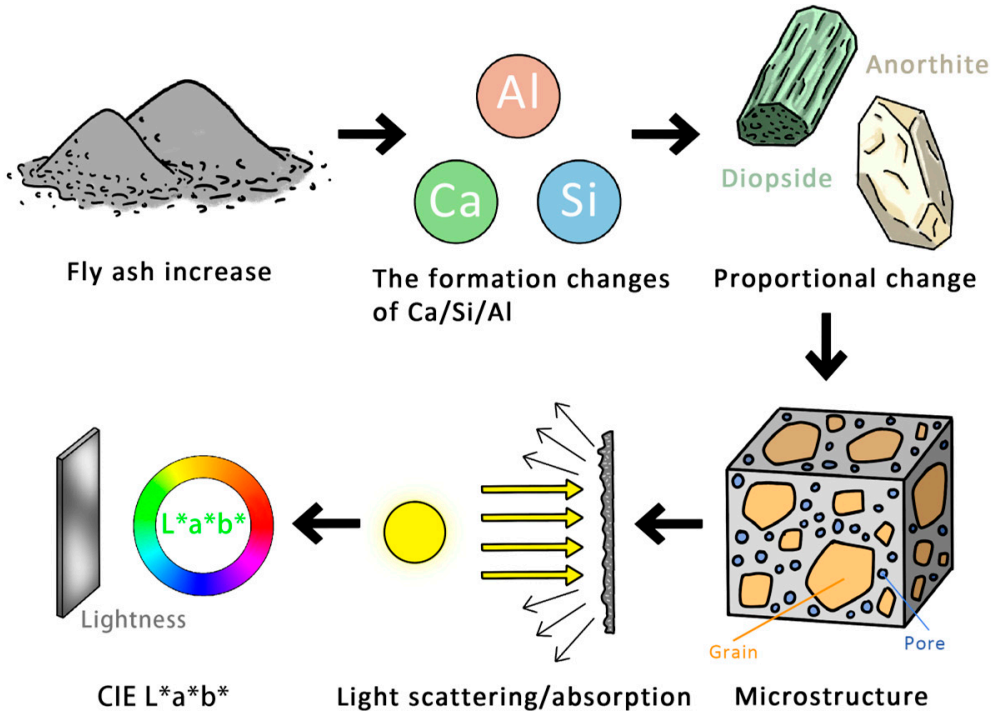

Figure 1. Conceptual roadmap of the study.

2. Experimental Design

2.1. Material Selection

To ensure the accuracy and reproducibility of experimental results, all solid waste raw materials are dried prior to use. The raw materials are in a naturally dried powder state. Subsequently, the materials are sieved through a 150-mesh screen to ensure appropriate particle size. Distilled water is then added drop by drop in a 1:1 ratio with the raw material while continuously stirring until a uniform glaze slurry is formed. Fly ash treated in this manner exhibits a certain degree of compositional stability. At the same time, this process minimizes the impact of particle size inconsistencies and impurities in the original fly ash on subsequent experiments.

This study utilized Class F fly ash, screened to 200 mesh, to optimize the reutilization of solid waste in ceramic glaze formulation studies. Silica fume was screened to 325 mesh, and desulfurization gypsum was processed into 45-micron particles. All three materials were sourced from Yantai Anda Environmental Technology Co., Ltd. in Shandong Province, China. Slag powder of S105 grade was chosen, featuring an approximate particle size of 10 microns. Coal gangue was chosen as powder screened to 325 mesh. Both materials were sourced from Lanke Water Purification Materials Co., Ltd. in Gongyi City, China. All experimental waste materials were sourced from the same batch of impurities. This minimizes the impact of batch-to-batch variations. The particle size of all solid waste materials was controlled prior to mixing. This process eliminates the influence of particle size variations on melting and microstructure. This study focuses on structural changes caused by variations in composition.

To further confirm the correlation between changes in the chemical composition and microstructure of the raw materials, we conducted X-ray fluorescence (XRF) analysis on the solid waste feedstock. The results revealed that the raw materials primarily consist of SiO_2, Al_2O_3, CaO, and MgO, providing a chemical composition basis for microstructure regulation.

On the other hand, testing glazes necessitates firing them with ceramic bodies, aligning with traditional ceramic production techniques. Following production protocols, we selected high-kaolin white clay for its high kaolin content. This choice was driven by two factors: 1. It is the traditional clay used in ceramic production. Utilizing high-kaolin white clay maximizes the replication of post-industrial production appearance characteristics. 2. High-kaolin white clay is characterized by exceptionally high whiteness, which facilitates observation of glaze color changes. The high-kaolin white clay material was sourced from Firefly Clay Materials Company in Jingdezhen, China.

2.2. Sample Preparation

The total solid waste content in this experimental formulation is 100%. We converted the proportions based on traditional ceramic production ratios. All solid waste is screened through a 150-mesh sieve before being put into use. Considering the chemical composition ratios of raw materials and traditional glazes, we determined a fly ash content of approximately 30%. Fly ash contains 50% silicon content, aligning with ceramic glaze composition. As a key variable, we individually blended fly ash at weight ratios ranging from 30% to 60%, ultimately preparing five distinct samples for subsequent experiments. Specific ratios are detailed in Table 2. Additionally, we indicated the primary chemical composition of the solid waste materials used: silica powder, coal gangue, and desulfurization gypsum. By adjusting the SF:FG ratio, we approximated the composition of traditional glazes. This further ensures the rationality of the formulation's origin.

Table 2. Solid waste feedstock mix ratios.

Code	Fly Ash (FA)	Blast-Furnace Slag (SL)	Silica Fume (SF)	Coal Gangue (CG)	Flue Gas Desulfurization Gypsum (FG)
G1	30%	10%	10%	40%	10%
G2	30%	20%	10%	30%	10%
G3	30%	30%	10%	20%	10%
G4	45%	30%	10%	5%	10%
G5	60%	20%	10%	0%	10%

All samples in this experiment were composed of solid waste materials in varying proportions totaling 100% by weight. The sample materials were mixed with distilled water at a 1:1 ratio to replicate traditional industrial ceramic production processes. This study employed bisque-fired kaolin clay and high-white clay as body materials [41]. The bodies were molded into identical 3 cm × 3 cm × 1 cm (before firing) specimens from the same batch. Utilizing traditional glazing techniques, a cross-hatch glazing method was applied three times to achieve an approximate glaze thickness of 3 mm, as illustrated in Figure 2. Subsequently, the samples were placed in an electric kiln for a 10 h firing cycle. The heating curve followed traditional firing protocols, reaching a maximum temperature of 1250 °C. Dimensional shrinkage was observed in the samples after sintering. The glaze and the clay body sintered simultaneously at high temperatures and contracted in unison, with their shrinkage rates being largely consistent. This is a common phenomenon in the ceramic sintering process and does not affect the research. Finally, the samples were allowed to cool naturally to room temperature.

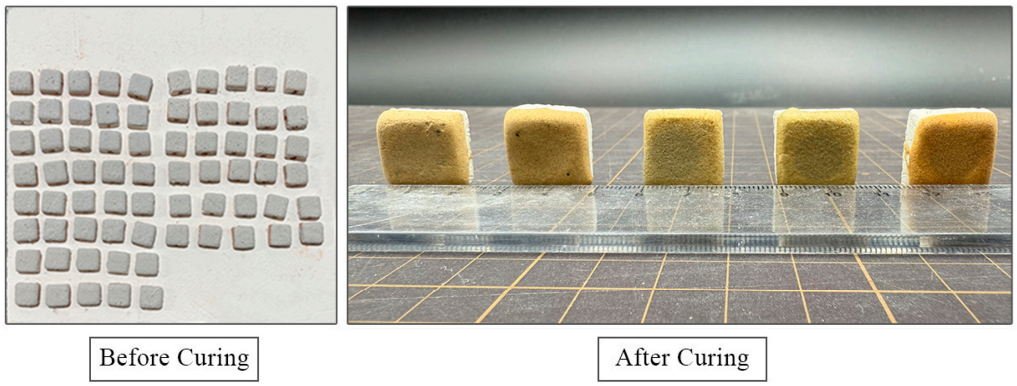

Figure 2. Comparison images before and after firing.

2.3. Sample Testing

2.3.1. SEM Testing

This study employed a scanning electron microscope (Regulus 8230, Hitachi, Japan) to examine the physical morphology of ceramic glazes. Concurrently, EDS was utilized to perform elemental analysis on multiple elements within the samples. This enables observation of the surface and cross-section of ceramic glazes, facilitating analysis of the microstructural composition of various solid waste materials within ceramics.

2.3.2. XRD Testing

X-ray diffraction (XRD) analysis was conducted using an XRD instrument (SmartLab SE) manufactured by Rigaku Corporation of Tokyo, Japan. The scanning range was 10–80°. This method provides a reveal of the network structure and oxide composition of ceramic glazes, enabling precise identification of the detailed roles played by crystals within them.

2.3.3. XRF Testing

We performed X-ray fluorescence (XRF) analysis on ceramic glaze samples using the ZSX Primus II from Rigaku Corporation, Japan. We identified the chemical elements present in the glazes. To improve readability of the analysis, we converted the individual elements to their oxide equivalents. This experiment facilitates the interpretation of chemical composition in the samples, thereby enhancing our understanding of their properties.

2.3.4. Color Testing

This study employed the LAMBDA 1050+ UV/Vis/NIR spectrophotometer from PerkinElmer, California, USA, for optical-visible spectroscopy testing. Samples were analyzed under visible light conditions spanning 380–780 nm with a 1 nm step size. Reflectance spectra were obtained using an integrating sphere + diffuse reflection method to measure the reflectance (R (%)) of ceramic glazes. In addition, this study used a colorimetric spectrophotometer to conduct L*A*B* optical color difference tests. In this system, L* represents the lightness of the sample being tested, while A* and B* indicate the color positions along the red–green and yellow–blue axes, respectively.

2.3.5. Repeatability Testing

To ensure scientific reproducibility and validate the experimental results, we conducted a duplicate experiment using newly fired raw materials (not from the same batch). The resulting color parameters were quantified using the CIE L*A*B* color space, supplemented with physical comparison images and commercial glaze comparison images.

2.3.6. Density, Water Absorption, and Porosity Tests

The water absorption, apparent porosity, and bulk density of five samples were determined using Archimedes' principle. The specific method involved measuring the dry weight of the samples, the weight of the saturated water, and the weight of the suspended samples. The saturated water was prepared using the boiling water method, in which the dry samples were immersed in distilled water and boiled for 10 min. The final weight was recorded after the samples had cooled naturally to room temperature [42].

2.3.7. Optical Aging Test

The purpose of this study was to verify whether the samples would exhibit color fading or other changes when exposed to prolonged sunlight. We set up a UVA340 UV aging chamber (Lianhui Cheng Technology Company, Shenzhen, China). to conduct the simulation. The setup utilized two 40W UVA340 UV lamps, with an operating temperature of approximately 30 degrees Celsius. Two parallel samples were selected for each test. One half of each sample was covered with an absorbent cloth strip. Finally, comparisons were made after 100 h of continuous UV exposure.

3. Results

The five physical samples exhibit a reddish-yellow color with a matte glaze surface texture. Table 3 lists the XRF compositions of the five samples. The results indicate that the composition consists primarily of SiO_2, Al_2O_3, and CaO, with SiO_2 having the highest content, followed by Al_2O_3, while the CaO content fluctuates significantly depending on the formulation. It also contains MgO, Na_2O, K_2O, Fe_2O_3, and TiO_2. This composition is derived from the same ratio of five types of solid waste. Fly ash contains high levels of SiO_2 and Al_2O_3. This provides the structural foundation for the glaze's silicoaluminate composition. Blast furnace slag contributes CaO and MgO. Coal gangue serves as a source of Al_2O_3. Desulfurization gypsum is added at a fixed rate of 10% to ensure a stable supply of CaO. By adjusting the proportions of these solid waste materials, the content of key oxides in the glaze is systematically controlled. For example, from G1 to G3. Increasing the amount of blast furnace slag while reducing gangue content from G1 to G3 resulted in a shift from a high Si-Al to a Ca-Mg phase. This enhances glaze solubility and alkalinity. From G3 to G5, Al_2O_3 shows a trend of first decreasing and then increasing, while Fe_2O_3 increases with the addition of fly ash. These results indicate that by adjusting the proportions of fly ash, blast furnace slag, coal gangue, silica powder, and desulfurization gypsum, systematic control of key oxides such as SiO_2, Al_2O_3, CaO, MgO, and Fe_2O_3 in the glaze composition has been achieved.

Additionally, we note that G1, G2, and G3 contain trace amounts of NiO, while G3 exhibits a high concentration of 3.2 wt%. The Fe_2O_3 content in G3 is 0.28%, significantly lower than in other samples. Moreover, G2, G4, and G5 contain measurable amounts of MnO.

Then, we utilized SEM to scan and analyze five samples individually, observing their microstructural features to examine the effects of different solid waste types in ceramic glazes. We examined the samples' characteristics at high, medium, and low magnifications. As shown in Figure 3, SEM scans at 1000× magnification revealed a coexisting structure of plate-like and spherical particles in all G1–G5 images. However, each sample exhibited slight differences: G1 and G2 contained relatively more voids and pores, along with a large agglomerate and clusters of fine particles. The presence of incompletely reacted frameworks resulted in a rougher appearance and a stronger sense of crystal accumulation.

Table 3. Chemical composition of raw materials (XRF).

w %	G1	G2	G3	G4	G5
SiO_2	45.14	42.99	39.86	42.22	44.61
Al_2O_3	25.40	24.91	21.63	19.86	22.65
CaO	18.22	20.39	27.89	27.60	20.08
MgO	1.08	1.53	2.85	3.00	1.35
Na_2O	0.47	0.55	0.59	0.47	0.59
K_2O	1.02	0.17	0.55	0.45	1.34
Fe_2O_3	4.87	4.83	0.28	3.31	5.57
TiO_2	2.88	2.75	2.12	2.24	2.81
MnO		0.18		0.28	0.13
ZnO	0.12	0.11	0.11	0.11	0.19
ZrO_2	0.11	0.13	0.09	0.06	0.06
Cr_2O_3	0.11				
NiO	0.04	0.04	3.20		
CuO			0.04	0.03	0.04
V_2O_5			0.19		
P_2O_5	0.11	0.13	0.08	0.12	0.12
SO_3	0.13	0.17	0.16	0.03	0.09
Cl	0.17	0.17	0.24	0.07	0.18
Rb_2O	0.08	0.05	0.04	0.05	0.13
SrO	0.06	0.08	0.09	0.08	0.05
Y_2O_3		0.01	0.01		
Nb_2O_5		0.02	0.02	0.01	0.02

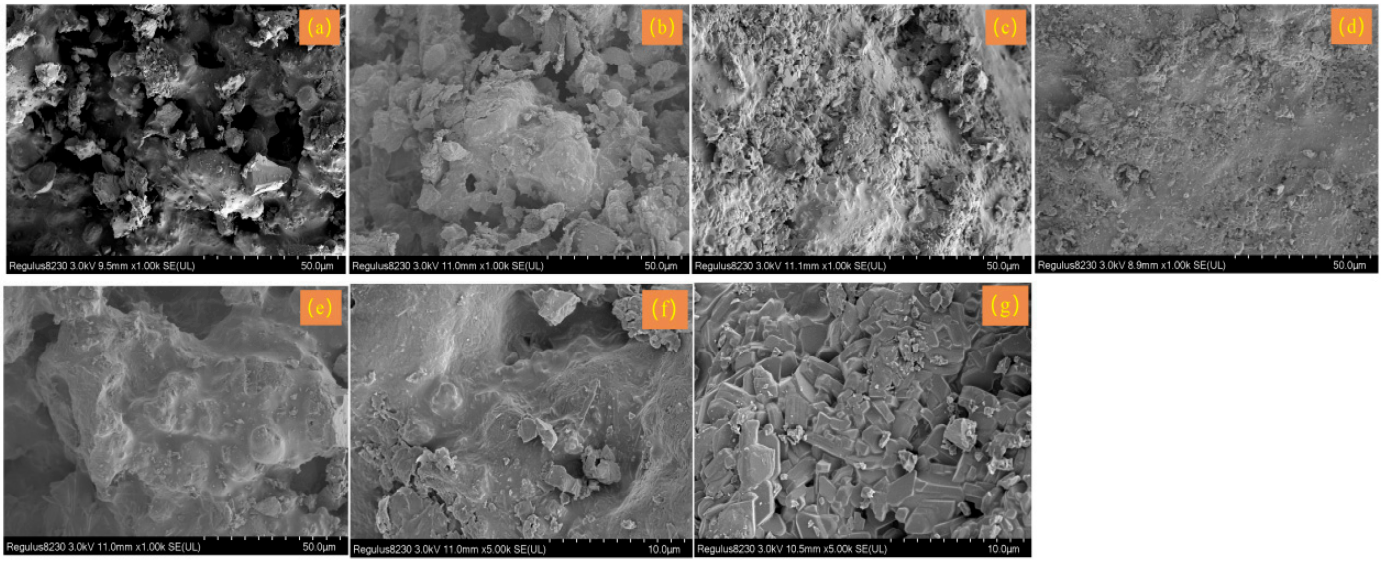

Figure 3. SEM scan photograph. (**a**–**e**) represent G1 to G5 in 1000×. (**f**,**g**) represent G2 and G3 in 5000×.

Figure 3f shows the G2 sample at 5000× magnification, revealing small rod-like crystals measuring 10–20 μm that have grown out from the glass phase. Combined with the EDS mapping shown (Figure 4) in a and b, dark regions appear in the Si and Ca element maps. These primarily occur in areas with higher porosity within the G1 and G2 samples. Additionally, both Si and Ca exhibit varying degrees of elemental clustering. This phenomenon may result from incomplete melting of raw materials during sintering or the presence of small, unreacted solid waste particles distributed on the surface. This observation is corroborated by SEM characterization. Fe elements show uniform distribution with low density, which corresponds to the material's uniform color and pale yellow appearance.

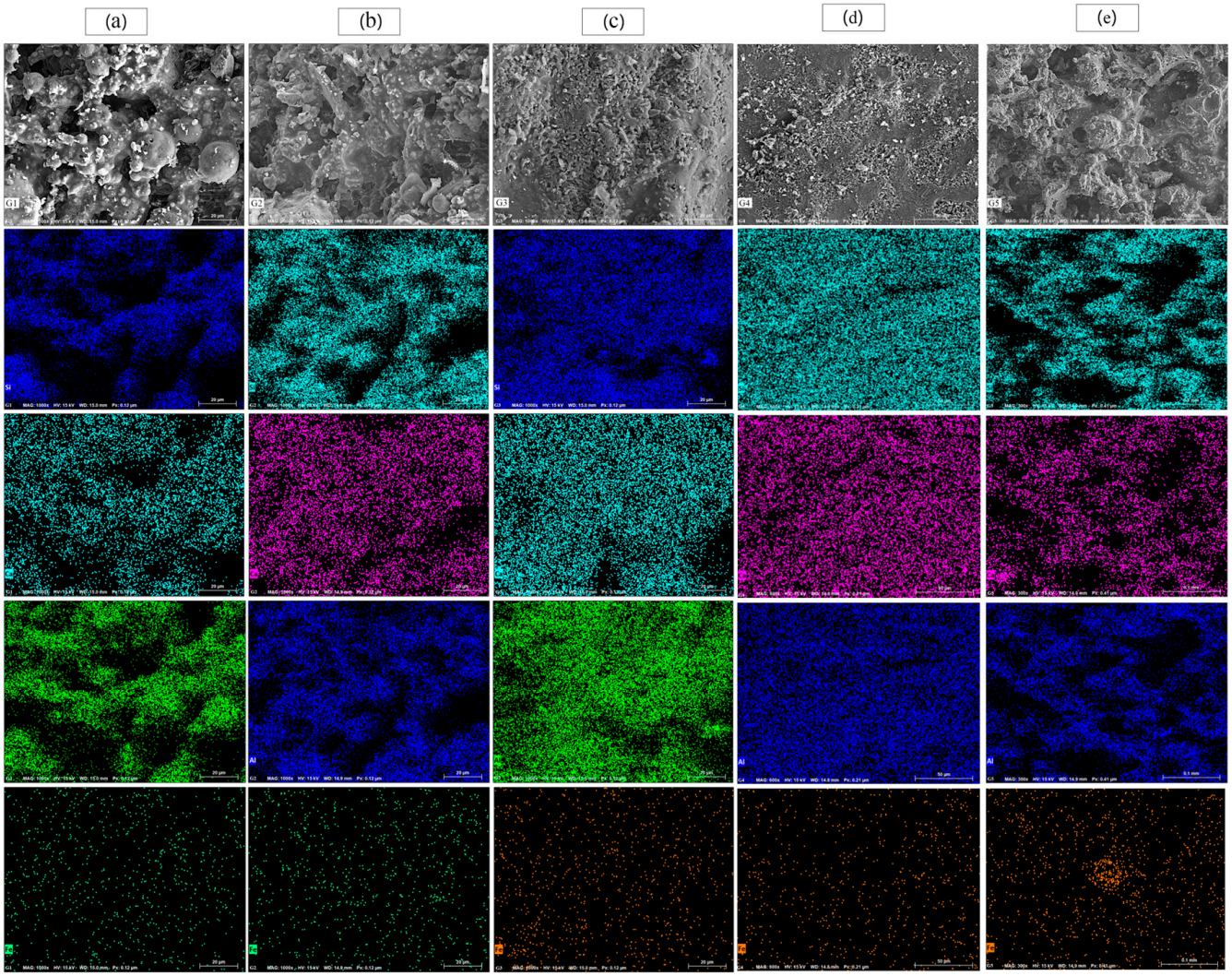

Figure 4. EDS element distribution maps of G1–G5. (**a**–**e**) show the elemental distributions of Si, Ca, Al, and Fe in G1 to G5.

Table 4 presents the atomic percentage data for samples G1–G5. It is evident that all samples are dominated by Si and Al elements, confirming the presence of a luminosilicate glass crystal matrix system. Notably, samples G1 and G3 exhibit elevated Ca values, indicating the potential formation of anorthite.

Table 4. Atomic percentage data for G1–G5.

	G1	G2	G3	G4	G5
C	6.02	7.85	7.15	20.83	6.38
O	54.09	55.71	53.56	49.14	55.46
Na	0	0	0	0.47	0.64
Mg	1.20	0.88	1.47	0.56	0.75
Al	12.29	11.76	13.24	11.12	13.00
Si	21.21	20.05	20.11	15.31	20.41
Ca	4.07	2.39	3.56	1.94	2.48
Fe	1.10	1.37	0.90	0.62	0.88

G3 exhibits extensive accumulation of block-shaped crystalline aggregates. As shown in Figure 3b, these crystals become more discernible at 5000×, with sizes ranging from approximately 10 μm to 20 μm. Their surfaces appear rough, and the aggregates exhibit

significant thickness. This indicates that crystalline precipitation occurs more frequently in G3, imparting a frosted texture to the surface. As shown in Figure 4c, the distribution of Si and Al elements exhibits continuity and coverage. This indicates that G3 possesses a more continuous Si–O network, with Ca acting as the primary fluxing agent. This may relate to the high-temperature coordination environment of the glass powder raw material, thereby forming a more stable glass phase continuum. Fe element distribution is generally low overall. Sample G3 contains NiO and has a low Fe_2O_3 content, combined with the presence of dense crystalline precipitates in its microstructure. These factors may have collectively influenced the sample's color, giving it a yellowish-green hue.

As shown in Figure 4, EDS mapping reveals that G1 exhibits fewer voids than G2, lower porosity, and surface undulations less than 5 μm, presenting continuous and smooth characteristics similar to a glass phase. The EDS map for Al shows dense and uniform distribution with virtually no dark zones. The Ca EDS map exhibits similar elemental distribution patterns, indicating significant Ca involvement in the firing process. Fe distribution is uniform with content comparable to G1 and G2 polymerization levels, suggesting the sample should exhibit a yellow color.

On the other hand, G5 exhibits a rounded, blunt pore morphology with an average pore size of approximately 15 μm, which may result in a coarse glaze texture. Al elements display a skeletal-like distribution pattern with particle sizes ranging from 30 to 50 μm. The EDS spectrum for Ca elements shows a distribution pattern similar to that of Si and Al. The EDS spectrum for Fe elements shows Fe in agglomerated clusters, with cluster sizes of approximately 20–40 μm. This suggests that G5 may exhibit color darkening caused by Fe elements and could potentially display a texture effect resembling "black holes".

Archimedes-based values were used to verify the differences in the overall porosity, water absorption, and surface area of the samples. This was done to further validate the reliability of the SEM results. As shown in Figure 5, the overall data for the five samples are similar, indicating that they belong to the same category. It is worth noting that G5 has the highest porosity, reaching 16.67%. This is consistent with the features observed via SEM. Additionally, G4 and G3 are generally similar. However, G4 has a slightly larger surface area than G3, indicating a denser structure. This is consistent with the previously observed characteristics.

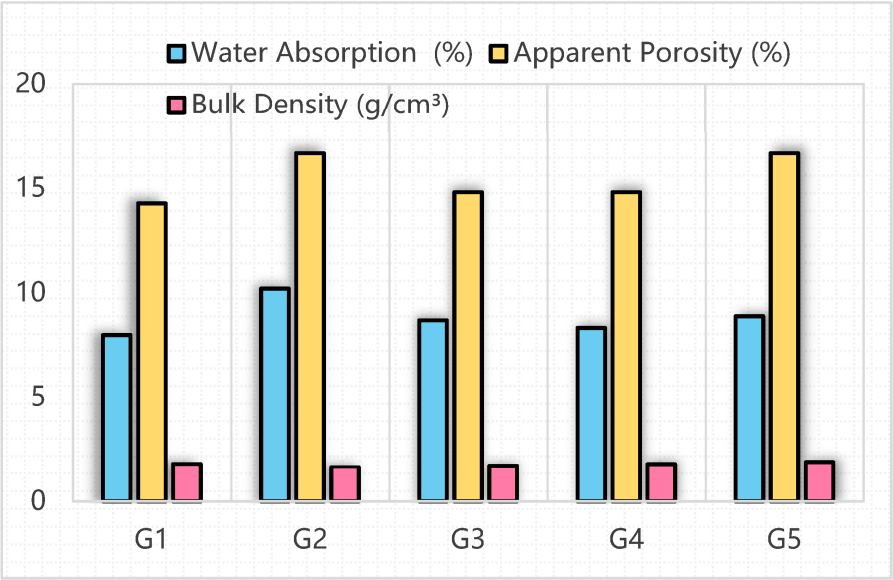

Figure 5. Water absorption, apparent porosity (AP, %), and bulk density (BD, g/cm^3) of G1–G5.

Figure 6 analyzes the structural characteristics of five samples and the relative effects of crystallization and solid waste on synthesis efficiency. Changes in the proportions of Al, Si, and Fe oxides introduced by solid waste materials such as fly ash, silica powder, and nickel-containing slag can lead to the formation of specific crystalline phases in the glaze and alter its crystallinity. When the Al_2O_3 content of the primary phase increases, it promotes the precipitation of the mullite phase, while SiO_2 exists in the form of quartz or stishovite. Under reducing atmospheres, Fe_2O_3 forms hematite; in silicon-rich systems, it may form olivine. In the presence of NiO, nickel silicate (Ni_2SiO_4) or nickel–iron spinel ($NiFe_2O_4$) is formed.

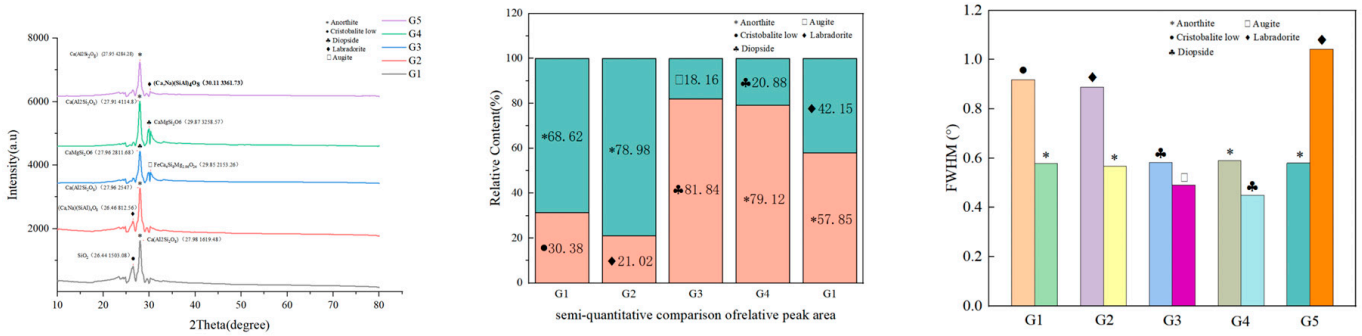

Figure 6. Phase analysis of G1–G5 (**a**) XRD patterns of G1–G5. (**b**) Semi-quantitative comparison of relative peak area of G1–G5. (**c**) FWHM of relative peak area of G1–G5.

Increasing the fly ash content by 20% leads to an increase in the viscosity of the glaze melt, which inhibits crystal growth. However, the overall crystallinity of mullite follows a trend of first increasing and then decreasing; an appropriate amount of fly ash promotes the formation of microcrystals. Excessive fly ash inhibits crystal growth due to excessive viscosity, causing crystallinity to decrease instead. An increase in Fe content leads to the formation of iron oxide phases via Fe^{3+}, which raises local crystallinity but tends to result in a rough glaze surface. An excess of silica powder promotes the precipitation of quartz phases, increasing crystallinity and yielding a translucent, smooth glaze surface. The key to achieving a matte finish lies in the fact that when fly ash is increased by 20%, the resulting crystallinity may affect diffuse reflection, thereby influencing the formation of the matte texture. The XRD patterns reveal that all five samples exhibit a ceramic crystal structure dominated by plagioclase (anorthite–labradorite solid solution), with the main peak positioned around 27.9. This indicates that after firing, the solid waste forms an aluminosilicate dominated by CaO–Al_2O_3–SiO_2 in the glaze, with plagioclase-type crystals precipitating out.

Specifically, the main peak of G1 and G2, anorthite (PDF 98-0093), is at 27.98, accompanied by a prominent secondary peak of cristobalite (PDF 98-0178) and labradorite (PDF 98-0272). This indicates that while a portion of the Al-Si has dissolved into the glass phase, refractory crystals remain precipitated. This pattern suggests both samples exhibit characteristics of high refractoriness and viscosity. On the other hand, the main peaks for G3 and G4 are diopside (PDF 98-0197) and anorthite (PDF 98-0093), respectively, with both samples showing the presence of diopside and augite. Combined with XRF chemical composition data, this pattern indicates that as CaO and MgO increase, both samples form high Ca–Mg pyroxene crystallization characteristics. This may lead to microcrystalline growth, consistent with SEM micrographs. It likely contributes to the presence of smooth, crystalline glaze. G5 exhibits simpler results, showing anorthite (PDF 98-0093) as the dominant peak without pyroxene or mullite. Ca-Mg content has decreased, returning the sample to plagioclase and SiO_2 crystallization characteristics.

G5 exhibits diffraction characteristics in the region above 30°, confirming that all samples possess crystalline structures, as shown in Table 5. The G5 sample displays diffraction peaks in multiple high-angle regions, indicating it has formed more regular crystalline structures of pyroxene and calcium feldspar.

Table 5. XRD pattern data for G1–G5.

		G1	G2	G3	G4	G5
2Theta	main peak	27.98	27.96	27.96	27.91	27.95
	secondary peak	26.44	26.46	29.85	29.87	30.11
Matched Phase	main peak	Anorthite ($Ca.Al_2Si_2O_8$)	Anorthite ($Ca.Al_2Si_2O_8$)	Diopside ($CaMgSi_2O_6$)	Anorthite ($Ca.Al_2Si_2O_8$)	Anorthite ($Ca.Al_2Si_2O_8$)
	secondary peak	Cristobalite low (SiO_2)	Labradorite ($CaNa.SiAl.4O_8$)	1.47Augite ($FeCa_4Si_8Mg_2.96O_2$)	Diopside ($CaMgSi_2O_6$)	Labradorite ($CaNa.SiAl.4O_8$)
PDF number	main peak	98-0093	98-0093	98-0197	98-0093	98-0093
	secondary peak	98-0178	98-0272	98-0102	98-0197	98-0272

Figure 6b presents a semi-quantitative analysis of the relative crystal phase compositions of five sample groups (G1–G5) based on the relative integral areas of characteristic diffraction peaks, clearly illustrating the relationship between composition and crystal phase composition: G1 and G2 are dominated by plagioclase (primarily calcic plagioclase) as the absolute major phase, containing only small amounts of low-temperature quartz or lauzanite, reflecting structural characteristics of high refractoriness and high viscosity; in G3 and G4, due to increased CaO and MgO content, the crystal phases completely or partially transformed into pyroxene-dominated phases (diopside and orthopyroxene); notably, diopside accounted for as much as 81.84% in G3, providing a structural foundation for microcrystal growth; in G5, as Ca-Mg content decreased, the crystal phases completely reverted to plagioclase-type (calcite + labradorite), with no pyroxene phase formed. It restored the crystallization characteristics of aluminosilicate plagioclases; this result is fully consistent with the phase identification from XRD patterns, verifying the reliability of the semi-quantitative analysis strategy in highly amorphous glaze systems.

Figure 6c further characterizes the crystallinity and grain size of each phase based on the full width at half maximum (FWHM) of the characteristic peaks; a smaller FWHM indicates higher crystallinity and more intact grains. The FWHM of calcite in all samples remained stable at 0.56–0.59°, making it the primary phase with the most stable crystallinity in the system. The FWHM of pyroxene-type phases in G3 and G4 was significantly lower than that of the secondary phases; in particular, the FWHM of diopside in G4 was only 0.45°, the lowest value in the entire set of samples. This confirms that high Ca-Mg content induces the growth of highly crystalline microcrystals in pyroxene, which is the core structural reason for the smooth and lustrous glaze surface. The FWHM of the secondary phases (low-temperature quartz and plagioclase) in G1 and G2, as well as that of plagioclase in G5, were all >0.9°, indicating lower crystallinity than the primary phases. This is consistent with the structural positioning of these secondary phases.

Additionally, Figure 7 presents the ternary phase diagram for G1 to G5, illustrating the phase equilibrium relationships within the $CaO–Al_2O_3–SiO_2$ ternary system at 1523 K (1250 °C). The three vertices of the phase diagram represent the components CaO, SiO_2, and Al_2O_3, respectively, while any point within the diagram denotes a mixture system composed of varying molar fractions of these three elements.

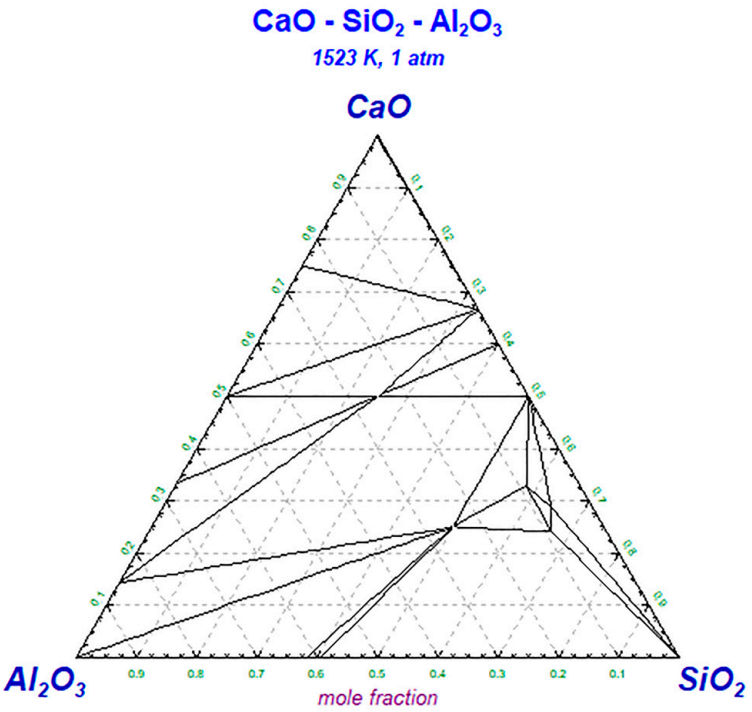

Figure 7. Ternary phase diagram, CaO:Al_2O_3:SiO_2 has a molar ratio of 56.08:101.96:60.08.

This further illustrates the equilibrium phases—such as calcite and pyroxene—that may form during high-temperature sintering of materials with varying fly ash content. It is evident that the samples control the precipitation of phases like pyroxene by increasing Ca and Si through SiO_2 and Al_2O_3 supplied by fly ash.

Overall, XRD analysis revealed the crystalline structure behavior and dissolution effects of solid waste in glaze materials. It was observed that blast furnace slag contains high levels of CaO and MgO, with their concentrations ranging from G1 to G3. The main XRD peaks gradually shifted from calcium feldspar ($CaAl_2Si_2O_8$) to diopside ($CaMgSi_2O_6$). This indicates that blast furnace slag promotes the formation of microcrystals while reducing the presence of refractory crystals and undissolved residues.

Additionally, fly ash has high SiO_2 and Al_2O_3 content. XRD analysis of samples G3 to G5 shows that the crystalline phase has reverted to calcite and quartz, while the pyroxene peak has weakened, indicating that fly ash enhances the precipitation of crystalline SiO_2 by increasing the Si:Al ratio, resulting in a single crystalline state. The findings comprehensively elucidate the structural mechanisms of solid waste incorporation in ceramic glazes. Together, they determine the types and relative proportions of crystalline phases in the glaze.

We analyzed the visible light spectra of the glazes on five samples using a visible spectrum analyzer. As shown in Figure 8, overall, the optical responses of all samples are largely consistent. This indicates that their fundamental optical characteristics are similar. Specifically, there is a strong optical response in the blue and cyan light bands between approximately 460 nm and 500 nm, with G2 approaching the peak. This may indicate a slightly warm yellow undertone. Additionally, significant differences were observed in the red wavelength region from approximately 650 nm to 690 nm, with G3 showing a notably higher response than the others, while G1 was significantly lower than G1, G4, and G5. This spectral segment reveals varying degrees of red influence, which may cause the samples to exhibit a greater tendency toward a yellow color deviation.

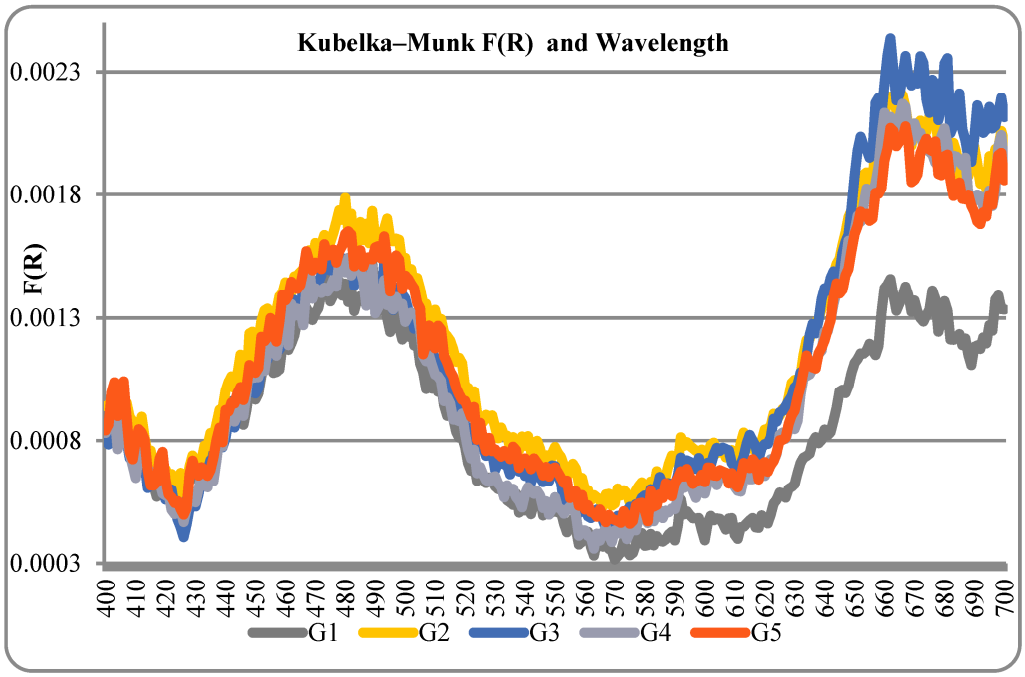

Figure 8. Diffuse reflection results for G1–G5.

To further verify the color of the glaze samples, we conducted another experiment. We reformulated the raw materials and fired the samples again. The color of the new batch of samples was quantified using the CIE L*A*B* colorimetric system. As shown in Figure 9a, the saturation of G1 to G5 ranges from 60.65% to 74.10%, with G1 having the highest brightness, reaching an L* value of 74.10%. G5 has the deepest color, with a saturation value of 60.65%. Additionally, Figure 9b displays the color results in the yellow direction. G5 exhibits the highest yellow value, reaching 31.04. G3 and G4 are similar, with values of 25.16 and 24.43, respectively. Among them, G1 is the weakest, with a value of only 25.16. As shown in the scatter plot in Figure 9c, all samples fall within the yellow–red region. G3 and G4 exhibit weaker red tones, which may be related to the cool color texture exhibited by these two samples.

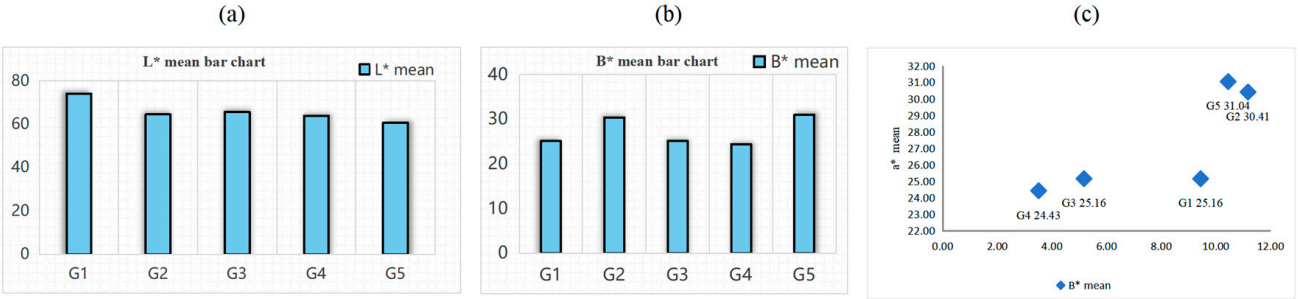

Figure 9. L*A*B* colorimetric results for the samples. (**a**) Lightness of the samples; (**b**) color results in the yellow direction; (**c**) scatter plots of the samples in the red and yellow directions.

Subsequently, we compared the samples from the two batches, as shown in Figure 10. We repeated the experiment. The results subsequently revealed that G1, G2, and G3 exhibited excellent color consistency in the repeated experiments. G1 and G3 demonstrated very high reproducibility, while G2, G4, and G5 showed some sensitivity. Figure 10 shows a color comparison between the first batch and the repeat batch of samples. The two sets of samples are displayed side by side to facilitate a visual comparison of their differences. The overall color trend and texture remained consistent. Therefore, both experiments

indicated that the two batches were highly similar, meeting the ideal expectations. G1 and G3 showed adequate repeatability with an error rate of approximately 1, but G4 exhibited some fluctuation in the B* value comparison.

Figure 10. Comparison of duplicate experiments involving two firings.

In addition, to explore further possibilities regarding the firing temperature of the samples, we fired the samples using a low-temperature glaze at 1100 °C. As shown in Figure 11, the glaze on the sample exhibited a non-crystallized surface. Various defects appeared on the glaze surface, including cracking, flaking, and a lack of color. This indicates that the current formulation is unable to form a ceramic glaze surface in the low-temperature range. The firing temperature remains limited to the high-temperature range.

Figure 11. Images of G1 through G5 being fired at 1100 degrees Celsius.

As shown in Figure 12a, half of the sample is covered with a light-blocking strip. This step is intended to provide a visual comparison of changes in color or texture following exposure. Figure 12b shows a comparison image taken after 100 h of continuous UV exposure. The experiment revealed that there were no changes in color or texture on either side of the sample. Therefore, it can be concluded that the sample exhibits a certain degree of stability.

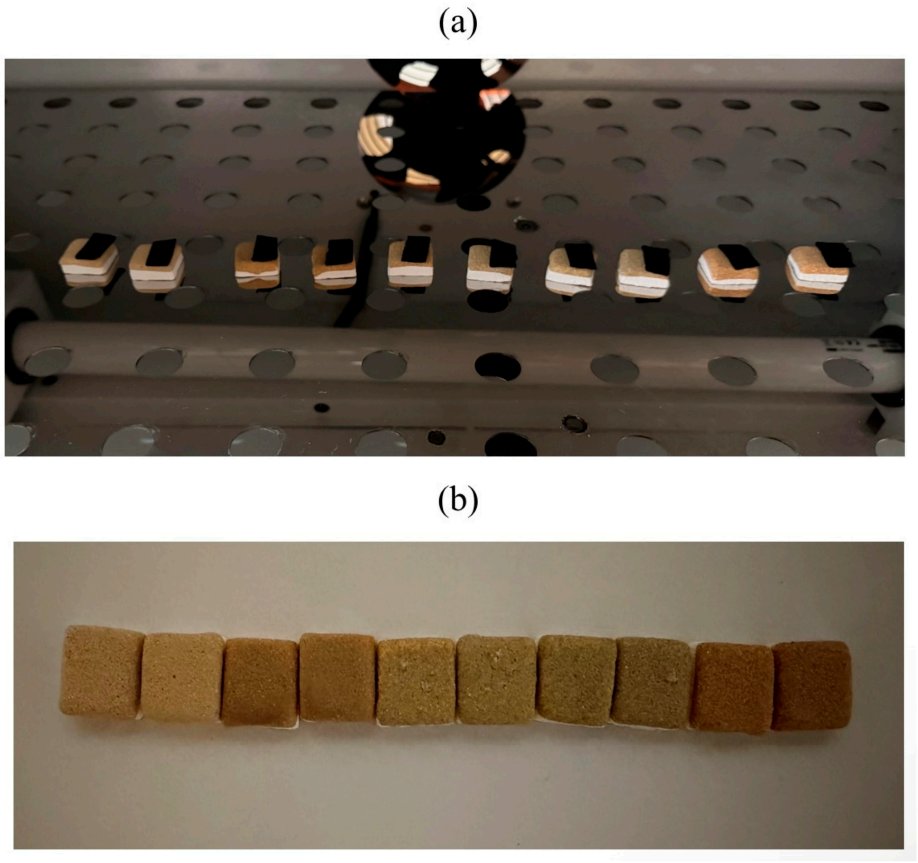

Figure 12. Comparison of optical aging test results for G1–G5. (**a**) figure of the object before the experiment. (**b**) figure of the result after the experiment.

Additionally, as shown in Figure 13 the left side displays samples G1–G5 fired in this study, while the right side features three commercially available glazes of different colors. As illustrated, both categories of glazes belong to the same category in terms of matte texture and style. This further indicates that the samples align with modern aesthetics and possess competitive commercial value.

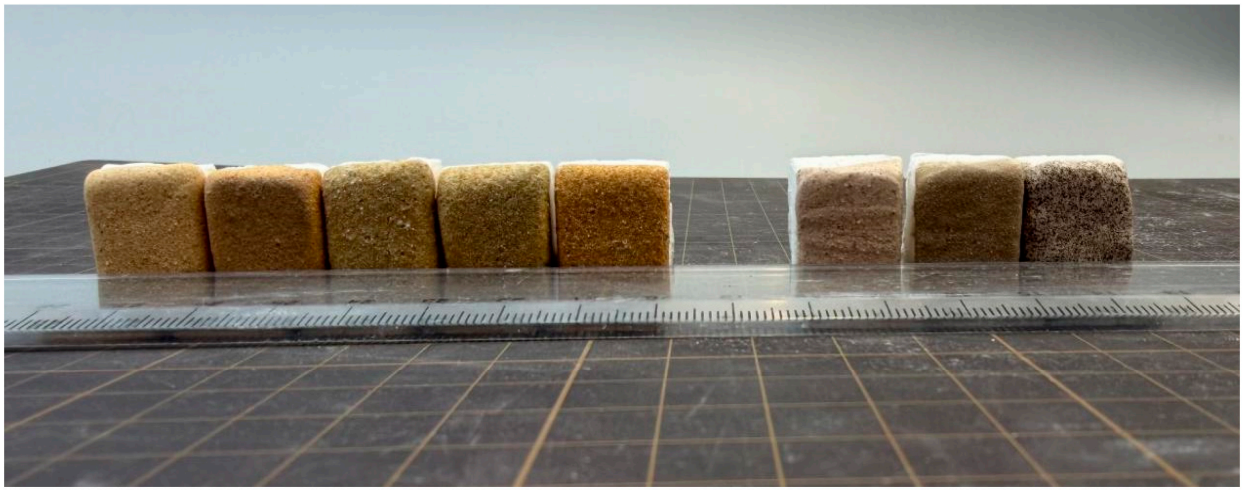

Figure 13. Comparison of conventional commercial glazes.

4. Conclusions

This study, grounded in traditional ceramic firing techniques, explores the use of fly ash (FA), blast furnace slag (SL), silica fume (SF), coal gangue (CG), and desulfurization gypsum

(FG) as raw materials for ceramic glazes. It analyzes the texture and color properties of these glazes. Through multiple characterization methods, including XRD, XRF, and SEM, we examined the crystalline changes, glass phase solubility, pore and precipitation ratios of different solid wastes during firing, along with their observable effects on ceramic glazes. Key findings are as follows:

1. G1–G5 all belong to the SiO_2–Al_2O_3–CaO system. By adding blast furnace slag and desulfurization gypsum, the CaO and MgO ratio can be adjusted, serving as the key source for crystal formation. In terms of texture, the porosity of the microstructure and the degree of crystal precipitation jointly influence the roughness of the glaze surface. XRF analysis indicates that when the CaO content is relatively low, as in samples G1, G2, and G5, the surface appears rough and porous; when the CaO content is relatively high, as in samples G3 and G4, the crystal distribution becomes denser, resulting in a relatively smooth glaze surface.
2. During firing, metals like Ca and Mg exhibit distinct states, thereby influencing the tendency toward either a "glass phase" or "crystalline phase precipitation." Additionally, the SiO_2 phase determines the Si-rich residue content and crystallization characteristics.
3. SEM results indicate that ceramic glazes from G1 to G3 exhibit relatively consistent physical appearances. Samples G4 and G5 demonstrate improved crystal continuity, reduced voids, and decreased unreacted waste material. XRD analysis confirmed that the solid waste samples contained primary crystalline phases such as anorthite and diopside. The crystal composition was influenced by variations in fly ash content, with increased fly ash addition causing the samples to revert to the crystallization characteristics of plagioclase and SiO_2.
4. The formation of both color and texture is related to the distribution state of microstructures, with texture being directly linked to the glass phase, voids, and precipitated crystals. The Fe_2O_3 content in G1 and G2 is higher than in G3, and G2 exhibits greater crystallinity. Iron is concentrated in the crystalline phase, resulting in a more pronounced reddish-yellow hue. G3 exhibits the most crystal precipitation, while G4 displays a more continuous and smooth surface. Additionally, the distribution of precipitated crystals and coloring elements directly correlates with glaze color. The NiO content in G3 is lower than that in G1 and G2. The G3 sample has a higher NiO content and a lower Fe_2O_3content, which together produce a cool-toned yellow–green luster.
5. The glaze color is jointly determined by the solid waste metal entering the glass phase and the crystal scattering intensity. Sample G5 exhibits a high Fe content (5.57 wt%) and good crystal continuity. Its color appears noticeably deep red to the naked eye. Samples G1 and G2 both have Fe contents around 4.8 wt%, but G2 shows more crystal precipitation. Visually, G2 exhibits a more reddish-yellow hue than G1.

By utilizing these solid wastes, we can reduce the depletion of primary ore mining while preserving the aesthetic appeal of ceramic glazes. Simultaneously, we have established a comprehensive design mechanism spanning chemical composition, phase structure, microstructure, and visual effects. This approach enables precise control over the otherwise unpredictable characteristics of glazes, making them suitable for everyday ceramic tableware, and commemorative items. This research not only advocates for environmentally conscious green design but also enhances economic efficiency.

5. Limitations

Although solid waste is now classified into grades, such as Grade F fly ash, variations in composition exist between different batches. This can lead to fluctuations in content, potentially resulting in glazes with differing effects. This study focuses on explaining

the patterns of microstructure from the perspectives of chemical elements and surface characteristics. However, it does not systematically discuss reaction differences related to particle size or the analysis of crystallization kinetics. Future research could further investigate the differences in reaction processes among waste materials of varying particle sizes, as well as the effects of crystallization kinetics on glaze structure under different firing temperatures. The phenomena primarily described in this chapter can be further validated quantitatively, such as through the Rietveld refinement method. Additionally, although this study did not conduct specific quantitative testing of mechanical properties, the continuous microstructure provides a basis for the stability of the glaze surface. Future research could explore metrics including gloss, hardness, adhesion, water absorption rate, porosity, and thermal shock resistance.

Author Contributions: Conceptualization, Y.H.; Software, L.C.; Formal analysis, Y.H.; Investigation, Y.D.; Resources, Y.D.; Writing—original draft, Y.D., L.C. and M.C.; Supervision, H.L.; Project administration, H.L. All authors have read and agreed to the published version of the manuscript.

Funding: This research was funded by the Hebei Natural Science Foundation (grant number E2024105053).

Institutional Review Board Statement: Not applicable.

Informed Consent Statement: Not applicable.

Data Availability Statement: The original contributions presented in this study are included in the article. Further inquiries can be directed to the corresponding author.

Conflicts of Interest: Author Yumeng Huang was employed by the Hebei Fine Arts Publishing House. The remaining authors declare that the research was conducted in the absence of any commercial or financial relationships that could be construed as a potential conflict of interest.

References

1. Trinca, A.; Segneri, V.; Mpouras, T.; Libardi, N.; Vilardi, G. Recovery of Solid Waste in Industrial and Environmental Processes. *Energies* **2022**, *15*, 7418. [CrossRef]
2. Zhao, T.; Zhang, S.; Yang, H.; Ni, W.; Shao, A.; Li, J.; Zhang, B.; Zhang, J.; Huang, X. Effects on high content of MSWI fly ash for the deterioration and immobilization performance of blast furnace slag-desulfurization gypsum-based binder. *Constr. Build. Mater.* **2025**, *463*, 139999. [CrossRef]
3. Hao, J.; Zhou, Z.; Chen, Z.; Shen, Y.; Fang, K.; Tang, F.; Xin, F.; Zhang, L. Synergistic mechanisms of steel slag, granulated blast furnace slag, and desulfurization gypsum in high-content steel slag-based cementitious backfill materials. *Int. J. Min. Sci. Technol.* **2025**, *35*, 1005–1018. [CrossRef]
4. Al-Khatib, I.A.; Kontogianni, S.; Abu Nabaa, H.; Alshami, N.m.; Al-Sari', M.I. Public perception of hazardousness caused by current trends of municipal solid waste management. *Waste Manag.* **2015**, *36*, 323–330. [CrossRef]
5. Diatmika, G.N.A.D.; Muka, I.K.; Suardina, I.N. Utilizing Sand as Glaze in Agung Glazinia Ceramics. *J. Aesthet. Creat. Art Manag.* **2022**, *1*, 59–70. [CrossRef]
6. Gülen, Ş.M.; Çöpoğlu, N.; Yılmaz, Y.B.; Karaahmet, O.; Cengiz, T.; Gökdemir, H.; Çiçek, B. TiO_2-based glass-ceramic coatings: An innovative approach to architectural panel applications. *Case Stud. Constr. Mater.* **2022**, *16*, e00805. [CrossRef]
7. Shackelford, J.F.; Doremus, R.H. (Eds.) *Ceramic and Glass Materials*; Springer: Berlin/Heidelberg, Germany, 2008; pp. 28–329. [CrossRef]
8. Pradell, T.; Molera, J. Ceramic technology. How to characterise ceramic glazes. *Archaeol. Anthropol. Sci.* **2020**, *12*, 189. [CrossRef]
9. Koroglu, L.; Peksen, C.; Ince, M.; Ayas, E. Cost-effective and eco-friendly transparent ceramic glazes for porcelain bodies. *J. Aust. Ceram. Soc.* **2023**, *59*, 1263–1269. [CrossRef]
10. Gol, F.; Cibuk, S.; Kacar, E.; Saritas, Z.G.; Yilmaz, A.; Arslan, M.; Sen, F. Evaluation of solid wastes in the manufacture of ceramic tableware glazes. *Ceram. Int.* **2022**, *48*, 15622–15628. [CrossRef]
11. Yuan, Q.; Robert, D.; Mohajerani, A.; Tran, P.; Pramanik, B.K. Utilisation of waste-to-energy fly ash in ceramic tiles. *Constr. Build. Mater.* **2022**, *347*, 128475. [CrossRef]
12. Khater, G.A.; Nabawy, B.S.; El-Kheshen, A.A.; Abdel-Baki, M.; Farag, M.M. Utilizing of solid waste materials for producing porous and lightweight ceramics. *Mater. Chem. Phys.* **2022**, *280*, 125784. [CrossRef]

13. Huasheng, L.; Weibin, D.; Xiaoli, S. From Industrial Waste to Art: Innovative Applications of Jun Porcelain Waste in Sustainable Environmental Design. *Environ.-Behav. Proc. J.* **2024**, *9*, 277–282. [CrossRef]
14. Ricciotti, L.; Occhicone, A.; Ferone, C.; Cioffi, R.; Roviello, G. Eco-design of geopolymer-based materials recycling porcelain stoneware wastes: A life cycle assessment study. *Environ. Dev. Sustain.* **2024**, *26*, 4055–4074. [CrossRef]
15. Dantas e Silva, M.d.F.; Costa, T.R.; Anjos, G.C.d.; Medeiros, R.L.B.d.A.; Nascimento, R.A.B.d.; Braga, R.M.; Melo, D.M.d.A. Sustainable ceramic coatings from Fe or Cr-impregnated oil shale ash: Microstructural, optical, and functional properties. *Surf. Interfaces* **2025**, *75*, 107722. [CrossRef]
16. Bayer Ozturk, Z.; Pekkan, K.; Tasci, E.; Yilmaz, S. The effect of granulated lead–zinc slag on aesthetic and microstructural properties of single-fired wall tile glazes. *J. Aust. Ceram. Soc.* **2020**, *56*, 609–617. [CrossRef]
17. He, B.; Du, Y.; Xu, H.; Ma, J.; Cheng, C.; Du, M. Synthesis of ceramic pigments with chromium content from leather waste. *Trans. Indian Ceram. Soc.* **2021**, *80*, 103–109. [CrossRef]
18. Yongvanich, N.; Soysom, P.; Ratkasemsak, W. Synthesis of zircon pigments from rice husk ash and their performance in ceramic glaze. *J. Met. Mater. Miner.* **2023**, *33*, 47–55. [CrossRef]
19. Du, Y.; Chen, M.; Wang, K.; Wang, T.; Wang, L. Integrating Fly Ash into High-Temperature Ceramic Glazes: Achieving Sustainability, Cost-Effectiveness, and Aesthetic Appeal. *Sustainability* **2025**, *17*, 8017. [CrossRef]
20. Yu, L.; Zhang, Y.; Wang, H.; Zhang, Z.; Shen, X.; Liu, H. Enhancing the sustainable production of cost-effective ceramics with high strength using kaolin, sewage sludge and blast-furnace slag. *Chem. Eng. J.* **2024**, *480*, 148184. [CrossRef]
21. Fu, F.; Hu, N.; Ye, Y.; Chen, G.; Guan, W.; Yang, S.; Li, Q. Production of high-value-added lightweight glass ceramics based on phosphorus tailings and coal gangue. *Ceram. Int.* **2024**, *50*, 16725–16735. [CrossRef]
22. Wang, H.; Chen, Z.; Meng, Z.; Liu, L.; Wang, X.; Qian, D.; Xing, Y. A novel and clean utilization of multiple solid wastes to produce foam glass-ceramic. *Constr. Build. Mater.* **2023**, *370*, 130711. [CrossRef]
23. Xu, A.-Y.; Li, H.-P.; Luo, K.-B.; Xiang, L. Formation of calcium sulfate whiskers from $CaCO_3$-bearing desulfurization gypsum. *Res. Chem. Intermed.* **2011**, *37*, 449–455. [CrossRef]
24. Gol, F.; Yilmaz, A.; Kacar, E.; Saritas, Z.G.; Ture, C.; Arslan, M.; Sen, F. Sustainable technology: Recycling roof tile waste in the ceramics industry. *Ceram. Int.* **2023**, *49*, 33773–33779. [CrossRef]
25. Montoya-Quesada, E.; Villaquirán-Caicedo, M.A.; Gutiérrez, R.M.d. New glass-ceramic from ternary–quaternary mixtures based on Colombian industrial wastes: Blast furnace slag, cupper slag, fly ash and glass cullet. *Boletín Soc. Española Cerámica Y Vidr.* **2022**, *61*, 284–299. [CrossRef]
26. Zhou, W.; Du, H.; Kang, L.; Du, X.; Shi, Y.; Qiang, X.; Li, H.; Zhao, J. Microstructure Evolution and Improved Permeability of Ceramic Waste-Based Bricks. *Materials* **2022**, *15*, 1130. [CrossRef] [PubMed]
27. Dong, X.; Han, F.; Yu, N.; Li, M. Preparation and characterization of novel spontaneous foam ceramics based on all-solid waste. *J. Alloys Compd.* **2024**, *976*, 173135. [CrossRef]
28. da Silva, R.C.; Pianaro, S.A.; Tebcherani, S.M. Preparation and characterization of glazes from combinations of different industrial wastes. *Ceram. Int.* **2012**, *38*, 2725–2731. [CrossRef]
29. Hui, T.; Sun, H.; Peng, T.; Liu, L.; Ding, W.; Liu, B.; Wang, C. Recycling of extracted titanium slag and gold tailings for preparation of self-glazed ceramic foams. *Ceram. Int.* **2022**, *48*, 23415–23427. [CrossRef]
30. Mendaci, S.; Boudeghdegh, K.; Roula, A.; Boulaiche, K.; Bouzidi, N. Effects of soda lime glass waste on the physical, mechanical and aesthetics properties of sanitary-ware glazes. *Sci. Sinter.* **2025**, *57*, 389–409. [CrossRef]
31. Lin, D.-F.; Wang, W.-J.; Chen, C.-W.; Lin, K.-L. Applying Mixture of Municipal Incinerator Bottom Ash and Sewage Sludge Ash for Ceramic Tile Manufacturing. *Materials* **2021**, *14*, 3863. [CrossRef]
32. İsraıl, L.İ. Mechanical and Microstructural Properties of Opaque Ceramic Tiles Glazed with some Industrial Wastes. *Glass Ceram.* **2022**, *79*, 340–347. [CrossRef]
33. Jagadeep, R.; Vignesh, R.V.; Sumanth, P.; Sarathi, V.; Govindaraju, M. Fabrication of fly-ash based tiles using liquid phase sintering technology. *Mater. Today Proc.* **2021**, *46*, 7224–7229. [CrossRef]
34. Shang, W.; Peng, Z.; Huang, Y.; Gu, F.; Zhang, J.; Tang, H.; Yang, L.; Tian, W.; Rao, M.; Li, G.; et al. Production of glass-ceramics from metallurgical slags. *J. Clean. Prod.* **2021**, *317*, 128220. [CrossRef]
35. Feng, X.; Lai, F.; Li, J.; Liu, Q.; Ren, S.; Yang, J. Crystallization behaviors and properties of Ti-bearing blast furnace slag-based glass ceramics with varying CaO/SiO_2 mass ratio. *J. Aust. Ceram. Soc.* **2022**, *58*, 597–605. [CrossRef]
36. Guo, X.; Zeng, M.; Yu, H.; Lin, F.; Li, J.; Wang, W.; Chen, G. Critical review for the potential analysis of material utilization from inorganic industrial solid waste. *J. Clean. Prod.* **2024**, *459*, 142457. [CrossRef]
37. Chen, C.; Zhang, Z.; Chen, P.; Huang, J.; Zhang, H.; Gao, D.; Li, T.; Chen, H. Coal fly ash based porous ceramic evaporator for highly efficient solar-driven seawater desalination. *Sep. Purif. Technol.* **2025**, *368*, 132999. [CrossRef]
38. Li, C.; Zhang, P.; Zeng, L.; Yu, L.; Li, D. Study on preparation of glass-ceramics from municipal solid waste incineration (MSWI) fly ash and chromium slag. *J. Build. Eng.* **2023**, *68*, 106080. [CrossRef]

39. Wang, H.; Chen, Z.; Meng, Z.; Liu, L.; Wang, X.; Xing, Y. Integrated utilization of coal gangue for synthesis of β-Sialon multiphase ceramic materials. *Ceram. Int.* **2023**, *49*, 11275–11284. [CrossRef]
40. Wang, H.; Zhang, H.; Zhao, P.; Wang, Y. Novel Low-Temperature Fabricated Coal Gangue-Based Porous Ceramics: Water Absorption/Retention Features and Their Application in Dryland Agriculture. *Sustainability* **2025**, *17*, 10111. [CrossRef]
41. Ho, J.W.I.; Quinn, P.S. Intentional clay-mixing in the production of traditional and ancient ceramics and its identification in thin section. *J. Archaeol. Sci. Rep.* **2021**, *37*, 102945. [CrossRef]
42. Cho, Y.; Cho, M.-G.; Ryu, J.-H.; Kim, J.-Y.; Choi, S.-H.; Shim, H.; Hong, M.-H.; Lee, D.Y. Influence of Machining, Polishing, and Glazing on Surface Properties and Biological Performance of Zirconia and Lithium Disilicate Dental Ceramics. *J. Funct. Biomater.* **2025**, *16*, 400. [CrossRef] [PubMed]